PhotoniX

RESEARCH Open Access

Naked-eye observation of water-forming reaction on palladium etalon: transduction of gas-matter reaction into light-matter interaction

Jongsu Lee[1,2], Eui-Sang Yu[3], Taehyun Kim[4], In Soo Kim[5], Seok Chung[4,6], Seung Jae Kwak[7], Won Bo Lee[7], Yusin Pak[1*] and Yong-Sang Ryu[8,9*]

*Correspondence: yusinpak@kist.re.kr; rongxiang82@korea.ac.kr

[1] Sensor System Research Center, Korea Institute of Science and Technology, Seoul 02792, Republic of Korea
[2] Department of Electrical and Computer Engineering, Seoul National University, Seoul 08826, Republic of Korea
[3] Smart Materials Research Section, Electronics and Telecommunications Research Institute, Daejeon 34129, Republic of Korea
[4] Department of Micro/Nano Systems, Korea University, 02841 Seoul, Republic of Korea
[5] Nanophotonics Research Center, Korea Institute of Science and Technology, Seoul 02792, Republic of Korea
[6] School of Mechanical Engineering, Korea University, Seoul 02841, Republic of Korea
[7] School of Chemical and Biological Engineering, Seoul National University, Seoul 08826, Republic of Korea
[8] Interdisciplinary Program in Precision Public Health, Korea University, Seoul 02481, Republic of Korea
[9] School of Biomedical Engineering, Korea University, Seoul 02481, Republic of Korea

Abstract

Palladium is the most prominent material in both scientific and industrial research on gas storage, purification, detection, and catalysis due to its unique properties as a catalyst and hydrogen absorber. Advancing the dynamic optical phenomena of palladium reacting with hydrogen, transduction of the gas-matter reaction into light-matter interaction is attempted to visualize the dynamic surface chemistry and reaction behaviors. The simple geometry of the metal-dielectric-metal structure, Fabry–Perot etalon, is employed for a colorimetric reactor, to display the catalytic reaction of the exposed gas via water-film/bubble formation at the dielectric/palladium interface. The adsorption/desorption behavior and catalytic reaction of hydrogen and oxygen on the palladium surface display highly repeatable and dramatic color changes based on two distinct water formation trends: the foggy effect by water bubbles and the whiteout effect by water film formation. Simulations and experiments demonstrate the robustness of the proposed Fabry–Perot etalon as an excellent platform for monitoring the opto-physical phenomena driven by heterogeneous catalysis.

Keywords: Palladium, Hydrogen, Oxygen, Fabry–Perot resonators, Colorimetric sensors, Water-forming reaction

Introduction

Color is an intuitive and powerful visual method for conveying distinguishing information. It is highly advantageous to detect and monitor molecular reactions via color variation without imaging instruments. In this sense, structural coloration and its dynamic color change assisted by nanotechnology provide a naked-eye view of nano/microscopic molecular interactions [1–5]. They showed selective manipulation of light scattering/absorption and reversible coloration in the visible spectrum (400–750 nm) in response to external stimuli including temperature [6], strain [7], moisture [8], biochemical molecules [9], gas [10], etc. Meanwhile, gas-matter interfaces where atomic-length-scale reactions via heterogeneous catalysis and surface chemistry (i.e. adsorption, diffusion,

rearrangement, nucleation, transfer, or inter-atomic reactions) occur are of interest for accumulating scientific knowledge for advancing science and meeting industrial demands.

As climate change and indoor air quality management become paramount, dynamic structural coloration by gas exposure is emerging as a vital future technology. Generally, gas adsorption onto metal oxides or polymers can trigger charge trapping, which induces global or local electron density changes [11]. Although reduction–oxidation reaction [12] or metal phase transitions including metal hydrides (MH_X) [13, 14] by gas absorption can shift the reflectance spectra, it is challenging to modify significant dielectric properties to reach dramatic coloration. In addition, direct tracking of an underlying atomic rearrangement and a reaction pathway in the course of gas-matter interactions is impossible in the visible spectra. This is because the feature size of such reaction components must be comparable to the resolution of the monitoring equipment: length scale-mismatching. Alternatively, extensive efforts for tracking the atomic/molecular interaction have been established by either computational simulations such as density functional theory (DFT) [15] or experimental proofs. Extravagant but state-of-the-art imaging techniques including scanning photoemission microscopy (SPM) [16], low-energy electron microscopy (LEEM) [17], ellipso-microscopy for surface imaging (EMSI) [18], reflection anisotropy microscopy (RAM) [19], transmission electron microscopy (TEM) [20], and their multiple combinations are the examples. However, we envision that such atomic-level observations can be visualized if atomic gas-matter reactions can be translated into light-matter interactions within a Fabry–Perot (FP) cavity, which can remove the stringent restrictions of state-of-the-art measurement techniques. A FP-induced-coloration can be obtained uniformly over a large area through a simple bottom-up process and offers exceptional color dynamicity within the visible spectrum [8]. In particular, since sophisticated physicochemical modulation of constituting layers of FP cavity lead to drastic color changes with respect to the external stimuli, thus, one could amplify the atomic-scale surface reaction behaviors into larger-scale and provide real-time tracking of the reaction pathway based on solely on colors.

Herein, we propose a FP etalon to couple the gas-matter reaction to the light-matter interaction by strategically designing a platform that confines selective gas adsorption and subsequent water-forming reactions in various chemical pathways. In a thorough understanding of the underlying principle of colorimetric changes in FP etalon devices, different gas-reactive pathways at the interface between a gas-permeable polymer film and palladium (Pd) metal were observed with drastic color variation. We found two distinct trends of color variations (i.e. color foggy effect vs. whiteout effect) in response to the predominating gas exposure because of the different behaviors of water-forming reactions (water bubble formation under O_2-dominated Pd surface and water film formation under H_2-dominated Pd surfaces) (Fig. 1). Based on knowledge of surface chemistry and sequential exotic optical phenomena by FP etalons, we reported the most advanced and practical approach for gas stimulus-induced dynamic optical coloration technology and investigated the underlying gas-matter physical/chemical interaction behaviors using simple spectroscopy and naked-eye monitoring methods. Based on this structure, we verified atomic-scale surface reactions with naked-eyes. Furthermore, this approach can fabricate scalable hydrogen gas sensors. The proposed platform is fundamental for

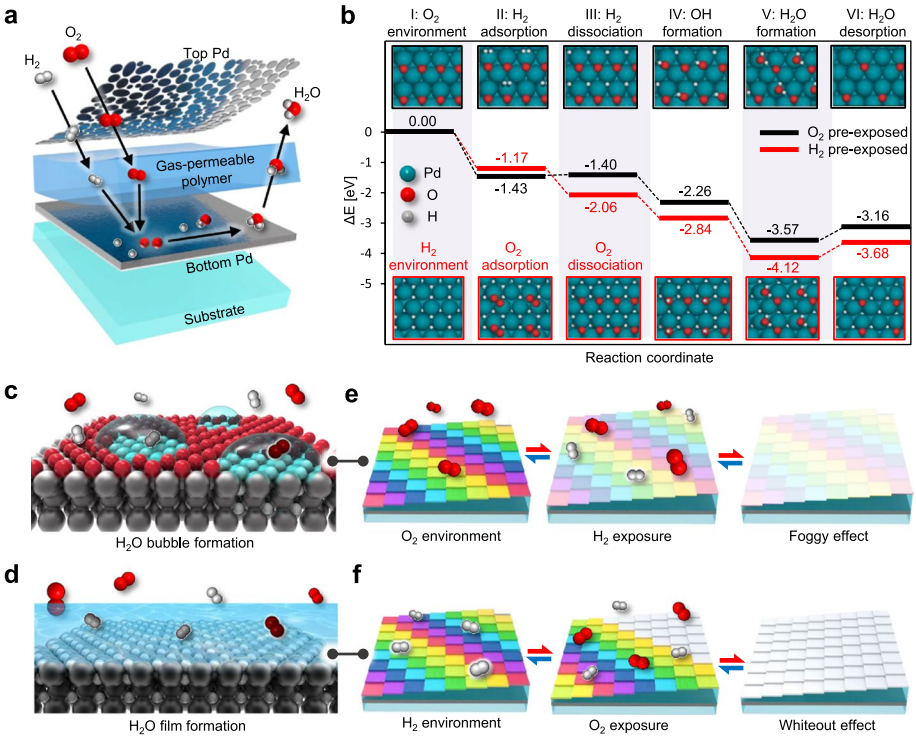

Fig. 1 Overall mechanism and phenomena of water-forming reaction at FP etalon. **a** Layer description of FP etalon and H_2/O_2 adsorption on the Pd surface undergoing the atomic-level catalytic reaction. **b** Energy profiles for dissociative adsorption of H_2/O_2 and H_2O formation/desorption on the Pd(111) surface initially exposed to O_2 (black) and H_2 (red). **c**-**f** Conceptual illustrations of atomical gas adsorption and sequential water-forming reactions inducing water bubble formation over the O_2-precovered (**c**) and H_2-precovered Pd surface (**d**) in response to H_2/O_2 gases exposure, resulting in optical foggy effect (**e**) and optical whiteout effect (**f**), respectively

understanding basic science and the fabrication of cost-effective gas sensors for industrial applications.

Result and discussion

Interfacial confinement of water-forming reaction at FP cavity for dynamic coloration

The FP resonance cavity, in which a gas-permeable polymer is sandwiched between the top and bottom Pd metals, was prepared to improve the performance of the gas-induced structural coloration (Fig. 1a). Only H_2 and O_2 penetrate and reach the polymer/bottom Pd interface where a catalytic reaction is expected. According to the pertinent literature, the dissociative adsorption of H_2 and O_2 occurs competitively on the Pd surface, forming H_2O [21–23]. Based on DFT calculations (Supplementary Note 1), exothermic steps for H_2O generation with different energy pathways are expected as a function of the surface chemistry of the Pd(111) surface (O- vs. H-covered Pd). The H-covered Pd surface shows preferred H_2 dissociation over the O-covered Pd surface due to the exothermic transition from state II to III (Fig. 1b). This led us to assume that different ratios or types of H_2O genesis are expected. For instance, the different H_2O genesis pathways and resultant distinct H_2O types (i.e. bubbles: Fig. 1c and film: Fig. 1d) may cause distinct optical phenomena (optical foggy effect: Fig. 1e and whiteout effect: Fig. 1f). Then, we can

monitor the atomic scales of surface catalytic reactions in color via light-matter interactions. Consequently, real-time and dramatic color changes in response to the alteration of the physical properties of the dielectrics (polymer insulating layer and newly formed water film) of the FP etalon can be realized by coupling the light-matter interaction of the FP cavity with the gas-matter reaction, which permits the water droplets/film and concomitant structural color change through gasochromic observation.

Water bubble formation at the polymer/Pd interface

Figure 2a shows the Pd-assisted catalytic reaction that produces water bubbles. At equilibrium, as the physisorption of O_2 on the Pd surface is thermodynamically more favorable than that of H_2, the surface coverage of adsorbed H_2 is relatively small [24]. High surface coverage of O_2 on the Pd surface interferes with the dissociative adsorption of H_2 involved with the correlation between the d-orbital of Pd and the s-orbital of H, degrading the efficiency of the water-forming reaction. When the coverage of dissociated H_2 on the Pd surface exceeds the threshold, spontaneous genesis of water film ($O_2 + 2H_2 = 2H_2O$) occurs at room temperature, experimentally proven under the critical pressure ratio of $O_2/H_2 < 2.5$ (Fig. 2a) [21]. However, for spatially H_2-covered spots

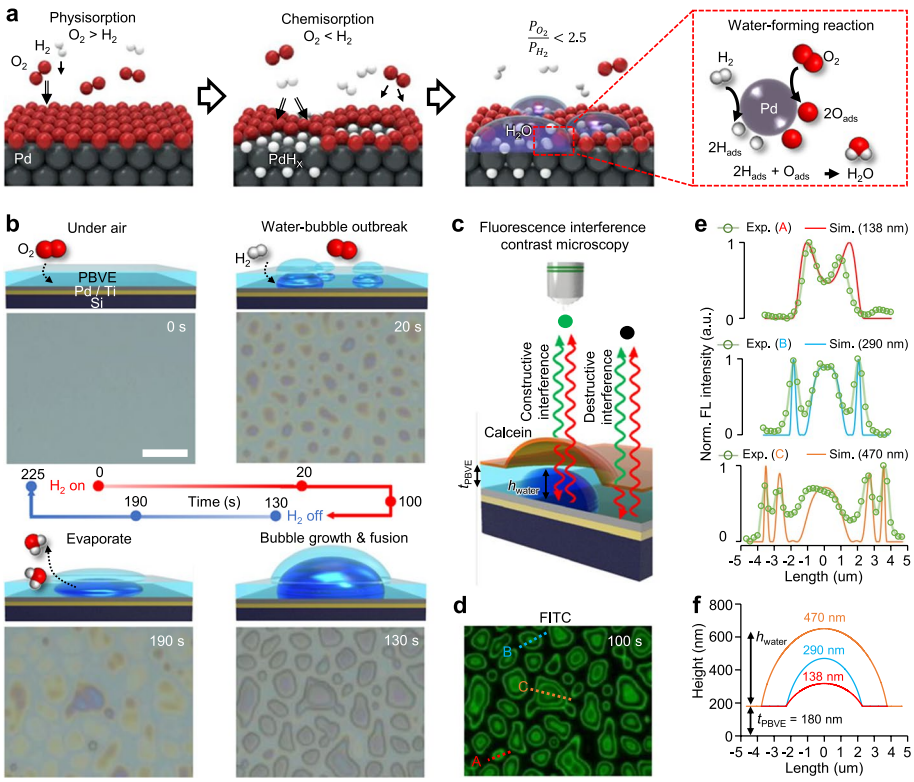

Fig. 2 Characterization of micron water bubble formation on Pd surface. **a** Schematic illustrations for understanding the underlying mechanism of water bubble formation on Pd surfaces after H_2/O_2 adsorption undergoing the atomic-level catalytic reaction. **b** Top-view microscopic images and corresponding side-view illustrations of PBVE-coated Pd surface under H_2 gas exposure at atmospheric condition. **c** Concepts and working principles of FLIC observation for micron water bubble formation at PBVE/Pd interface. **d** FL intensity of micrograph monitored using FITC filter (100 s). **e** Measured FL intensities from dashed lines of **d** (A: red, B: sky-blue, and C: orange) with simulated FL curves (solid-lines) with respect to the h_{water} modulations. **f** FL intensity-based simulation results of PBVE deformation by water bubble formation. Scale bar, 10 μm

surrounded by overwhelming O_2-covered area, the water-forming reaction will occur in the forms of 'water bubbles' discarding the possible scenarios of a nanometer-thick water film and their successive growths via coalescence processes. In addition, the H_2O evaporation rate should be suppressed and minimized than the H_2O generation rate to maintain the pre-formed H_2O bubbles. For this, the Pd surface was coated with a 180-nm thick perfluoro-(butenyl vinyl ether) (PBVE) film as a sieve layer with selective gas permeability only for O_2 and H_2 [25]. Oxygen permeability through a Pd-covering PBVE membrane is essential to trigger the water-forming reaction. As a control experiment, we compared the gas colorimetric behavior of another sample prepared using O_2-impermeable polymethyl methacrylate (PMMA) as a dielectric film. There were no water bubbles under identical H_2 conditions, confirming the role of dielectric films in water formation via selective gas permeability (Supplementary Fig. S1 and Supplementary Note 2).

To investigate the formation of water bubbles by H_2 adsorption at the PBVE/Pd interface, a sample with PBVE/Pd/titanium (Ti) (180 nm/10 nm/10 nm) on a silicon (Si) substrate was exposed to 10% H_2 in a gas chamber (N_2:O_2 = 4:1 as a carrier gas), and the dynamic water bubbles formation was monitored in real-time under a microscope (Fig. 2b). A Ti layer promoted adhesion between the PBVE and Pd films and suppress abrupt phase change (from α to β phase) causing Pd film deformation such as peeling and wrinkles [26]. Randomly positioned outbreaks and growth of micron H_2O bubbles, followed by coalescence between neighboring bubbles, were observed (< 130 s), which varies from previous studies of nanometer-thick transient water generation without a Pd-covering membrane [22, 23, 27]. After turning the H_2 supply off (> 130 s), we observed a gradual decrease in the water bubble volume and subsequent disappearance (225 s) equal to the initial state (0 s).

Three-dimensional (3D) PBVE deformation during the water-forming reaction was confirmed via fluorescence interference contrast microscopy (FLIC) [28]. For fluorescence (FL) visualization, a thin layer of calcein as the fluorescent dye was coated atop the PBVE surface, followed by 10% H_2 exposure (Fig. 2c). Interference-assisted alternative bright/dark patterns arise from the vertical movement of the dyes, and fluorescein isothiocyanate (FITC)-labelled calcein and the resultant fringe patterns allow an analysis of the height of water bubbles (Fig. 2d and Supplementary Video 1). Figure 2e shows the normalized FL intensities measured from Fig. 2d as a function of the water-bubble scanning length with corresponding simulation results. The intensity profiles of the fringe patterns along the dashed lines confirm that more fringes can be created as the exposure time or H_2 concentration increases. Tracking FL molecules via simulations revealed that the PBVE membrane swelling owing to the water bubble growth underneath the calcein layer experienced a height alteration of 138 nm (red), 290 nm (blue), and 470 nm (orange) during 100 s (Fig. 2e and f; Supplementary Fig. S2 and Supplementary Note 3).

Optical foggy effect by water bubbles induced light diffusion

This study realizes various color changes by reinforcing light-matter interactions based on the volume change of the dielectric layer. To boost the light-matter interaction, the FP resonator [29], underpinning the naked-eye observation of the water-forming reaction, was adopted by depositing another Pd layer on the PBVE surface. A

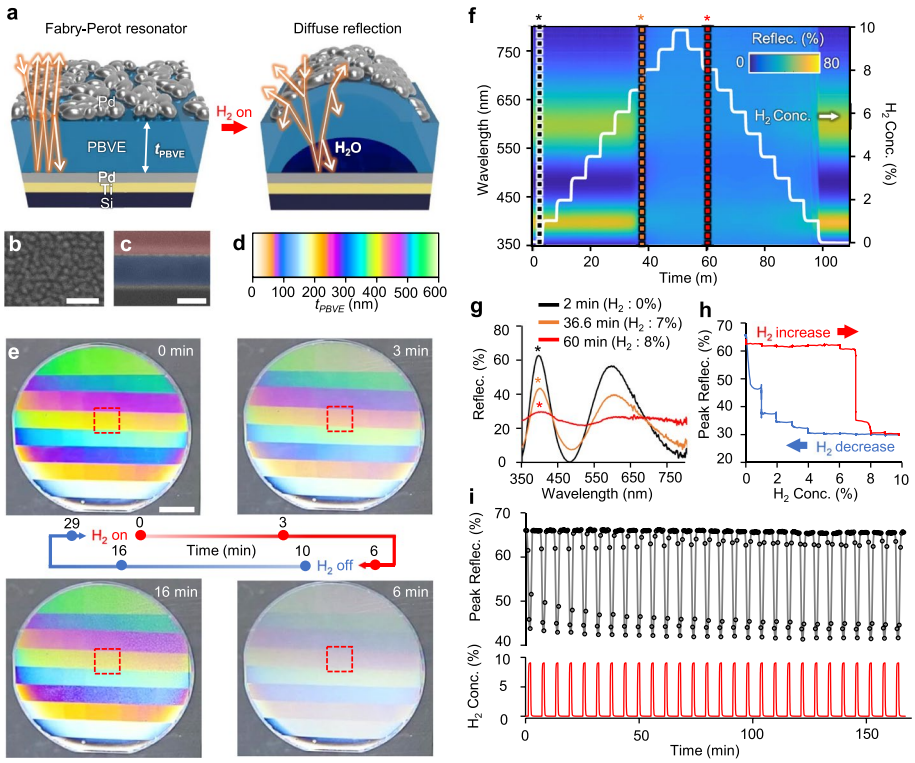

Fig. 3 Color change of Pd-PBVE-Pd etalon with varying H_2 concentration. **a** Schematic illustrations of FP etalon prior to (left) and post to (right) the water bubble formation with resultant optical effect. **b**, **c** SEM images of the etalon sample. Top-view- (**b**) and pseudo-colored side view images (**c**) after focused ion beam milling (red: epoxy coating layer, blue: PBVE). **d** Simulated reflection color gradient on the FP etalon with different thicknesses of the PBVE, t_{PBVE}. **e** Photographs of FP etalon on a 4-inch wafer under 10% H_2 showing color reversibility at atmospheric condition. **f** Measured reflection spectra as a function of H_2 concentrations (0–10%) at the red-dashed area of **e**. **g** Sampled reflection spectra (each color matches to dashed lines in **f**). **h** Alteration of an amplitude of reflectance peak while varying H_2 concentration. **i** Repeatability test of FP etalon undergoing H_2 exposure for 28 times over 2.5 h. Scale bar in **d**, 50 nm. Scale bar in **c**, 200 nm. Scale bar in **e**, 2 cm

metal-dielectric-metal (MDM) structure, known as the FP etalon, enables sensitive color variations as a function of physicochemical properties, such as the thickness and refractive index (RI) of the dielectric layer [30–33]. Thus, their modulation induced by water bubble formation and growth at the PBVE/Pd interface would cause a dramatic color shift. In addition, hemispheric water bubbles may cause diffuse reflection of incident light as they act as individual lenses (Fig. 3a).

Designing a perforated top metal layer with efficient transreflective characteristics is essential for generating the FP resonating effect. Compared to other metal nanoparticles having the optimum plasmonic enhancement in a few nano-meter size [34, 35], the optimum deposition thickness of 15 nm with a volumetric filling fraction of 0.45 for the nanoparticulated Pd layer was selected through experimental optimizations and a computational simulation to advance the FP resonance effect for producing wider range of color displays (Fig. S3 and Supplementary Note 4). The top-view (Fig. 3b) and side-view (Fig. 3c) scanning electron microscopy (SEM) images show that a 15-nm-thick Pd layer was deposited on the PBVE film. The FP etalons on a 4-inch Si wafer with varying dielectric PBVE thickness, t_{PBVE}, values from 0 to 590 nm at 10 nm intervals were controlled by

a delicate plasma etching process, showing excellent correspondence in reflection color trends with simulation results (Fig. 3d and e; Fig. S4 and Supplementary Note 5). The t_{PBVE} increases from the left-bottom corner (0 nm) to the upper-right corner (590 nm) (Supplementary Fig. S4). Figure 3e shows that reflection colors of the FP etalon turn discolored and eventually become foggy when exposed to 10% H_2 under atmospheric conditions. As predicted in Fig. 3a, diffuse reflection due to newly formed micron-water bubbles interrupts the FP resonance, thus resulting in foggy colors (bottom-right photograph of Fig. 3e, at 6 min), and this transition is fully reversible (Supplementary Video 2). After establishing that color transition occurs due to water bubble formation in the dielectric layer, we quantified the critical gas values that trigger color transitions. The reflectance spectra at the center yellow area (red-dashed square in Fig. 3e) were measured as H_2 concentration was gradually increased and decreased by 1% every 5 min (Fig. 3f). When H_2 concentration reaches 7%, nearly corresponding to the critical ratio of $O_2/H_2 = 2.5$, the waveform of reflectance over the visible range begins to flatten (lowering peaks and raising dips shown in Fig. 3g). Spectral peaks and dips also response to H_2 concentration from 2–6% with an average response time (t_{90}, a time required to reach 90% of the saturated reflectance) of 28.7 s when both top and bottom Pd layers become hydrogenated, but the calculated color difference (ΔE) is near 2.3 (just noticeable difference) (Fig. S5 and Supplementary Note 4) [36]. However, ΔE above 7% H_2 is greater than 40, and the response time to reach $\Delta E = 2.3$ is less than 5 s under $H_2 = 4\%$, which is known as a lower flammability limit [37].

Herein, several factors can be suggested to reduce the response time of Pd-based hydrogen color detection. First, the Pd nanocrystals with a specific orientation can speed up the absorption and dissociation of H_2 gas [38]. Second, alloying with sub-monolayer amounts of gold (Au) nanoparticles can be effective method for increasing the rate of hydrogen absorption kinetics by a factor of more than 40 when compared to pure Pd system [39]. Finally, regarding that the absorption rate is highly dependent to the number of remaining adsorption sites [40], a combination of Pd with high hydrogen-acceptable materials such as yttrium (Y) and magnesium (Mg) in the forms of composite thin film can be an alternative strategy for improving absorption speed.

By plotting the peak reflectance around 400 nm wavelength depending on H_2 concentration (Fig. 3g), the water-forming reaction vigorously occurred from 7 to 8% and then decreased from 4% (Fig. 3h). The rapid reduction in the peak reflectance over 7% H_2 indicates that the water bubble formation and coalescence are instantaneously accelerated at around a critical ratio of 2.5. The slow recovery of the peak reflectance with decreasing H_2 concentration is probably attributed to the thermodynamically unfavorable desorption of H_2O molecules at the Pd surface (endothermic transition from state V to VI in Fig. 1b). At 4% H_2, the recovery rate gradually increased because minuscule water bubbles (bottom left photograph of Fig. 3e, at 16 min) only existed. An H_2 concentration-dependent change in the peak reflectance (lowering peaks and raising dips) was continuously observed in multiple H_2 injection/purging cycles, demonstrating the excellent repeatability ($\geq 28\times$) of our FP etalon, considering that typical metal-hydride-assisted color displays showed limited ($\leq 20\times$) operating cycling numbers (Fig. 3i) [41]. Additionally, no mechanical deformation of the device was observed irrespective of the duration of the water-forming reaction (Fig. S6).

Multichromatic change by the water-film formation and following whiteout effect

O_2-predominated Pd surface promotes random water bubble formation under H_2 gas exposure (Figs. 2 and 3). Figure 1 shows that the Pd-dominated gas can determine the surface chemistry and resultant water formation types. We investigated the colorimetric changes in the FP etalon after preparing the H_2-predominated Pd surface before the O_2 gas supply and examined whether such different surface properties promote distinct forms of water products. In accordance with previous studies that a nanoscale water film could be formed when a Pd surface is entirely preoccupied with H_2 before the O_2 gas supply [23], the FP etalon was exposed to 10% H_2 for 5 min to induce full β-phase Pd hydride (PdH_X) and H_2-predominated Pd surface (Fig. 4a) [42], followed by 20% O_2

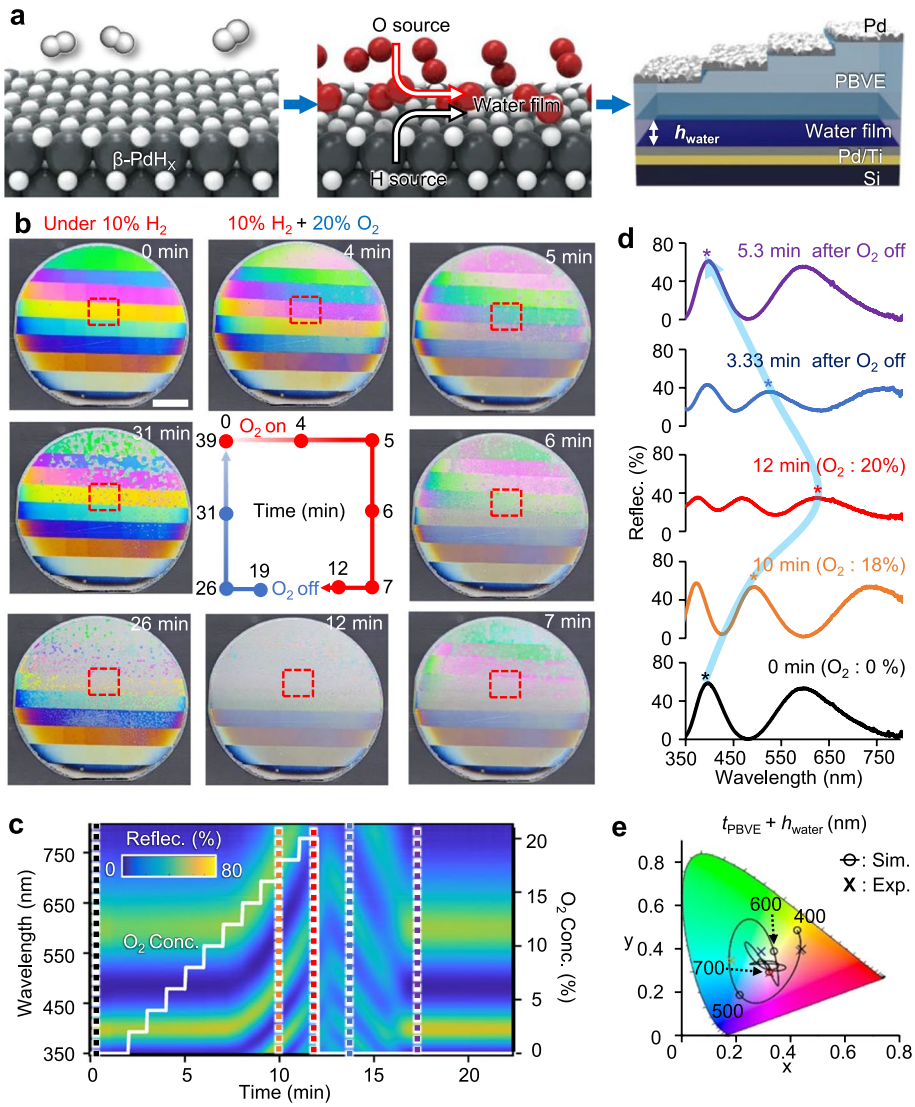

Fig. 4 Multichromatic change and whiteout effect by water film formation. **a** Schematic illustrations describing water-film formation on β-phase PdH_X surface. **b** Time-lapse photographs of the FP etalon under 10% H_2 followed by 20% O_2 exposure. **c** Measured reflection spectra as a function of O_2 concentrations (0–20%) at β-phase PdH_X surface (red-dashed area of **b**). **d** Sampled reflection spectra (each color matches to dashed lines in **c**). **e** CIE 1931 color map of the FP etalon depending on t_{BPVE} (400–1200 nm) (circles for simulation and 'X' for experimental results from **d**). Scale bar, 2 cm

gas supply. The uniform formation of nano-water film at the PBVE/Pd interface is useful in the optical interpretation since the RI of water ($n = 1.33–1.34$ in the visible range) is similar to that of PBVE ($n = 1.34$ at 550 nm and 1.333 at 1.55 um). Thus, generating a nanoscale water film underneath the PBVE layer can be simply interpreted as thickening the dielectric layer of the FP etalon, enabling multichromatic changes as a function of the water film thickness. Figure 4b shows reversible and drastic color changes in the 10% H_2 pre-exposed etalon under 20% O_2 gas exposure. Compared with the color changes above (Fig. 3), a rapid and dramatic color change was observed, producing an exotic optical whiteout effect in 10 min. In addition, reversible color recovery was completed within 20 min after cutting off the O_2 supply.

To elucidate the water-film thickness-based color variation on the FP etalon, we analyzed the time-lapse spectra at the center yellow area (red-dashed squares in Fig. 4b) with increasing O_2 concentrations up to 20% by 2% every 1 min (Fig. 4c and Supplementary Video 3). The red shift of the measured waveform was initiated at 12% O_2 concentration (8 min) and maximum before the gas cut-off (12 min). The red shift in the visible range is attributed to the increased effective thickness of the dielectric film (PBVE + water). A simulation was conducted by varying $t_{\text{dielectric}}$ to confirm the effect of dielectric film thickening on the color shift of the FP etalon (Supplementary Fig. S7 and Supplementary Note 6). Simulations verified that the measured spectral shifts arose from the dielectric thickening effect, that is, additional H_2O film formation below the PBVE layer. The second resonance peaks (Fig. 4d), extracted from the reflection spectra (Fig. 4c), show not only a red shift but also an overall decrease in magnitude (Fig. 4d). From an optical analysis perspective, the thickening of the dielectric film caused the coexistence of higher-order resonances in the visible range, resulting in the whiteout of the FP etalon (Fig. 4e).

Scalable and transparent display for gas detector via water-forming reaction

Implementing the water-forming reaction at the gas-permeable polymeric membrane and Pd interface can cause substantial innovations in various hydrogen applications. Forthcoming commercial coloration device technology must fulfil both aesthetic elements and outstanding performance and must be prepared in a facile fabrication process over various solid supports (such as a transparent and flexible substrate) in a scalable manner. Furthermore, it would be beneficial if the MDM could comprise various dielectric and metal components with identical functions. Respectively, our proposed technology can realize various theme colors by simply controlling the thickness of the metal and polymer layers. Furthermore, delicate and aesthetic drawings or patterns of a few microns can be easily fabricated via compatible semiconductor processes, meeting demanding industrial needs with high prospects for commercialization and technological standardization.

By depositing all metal layers through a shadow mask, a flower-patterned etalon (f-etalon) was prepared on a 2.5 cm × 2.5 cm glass substrate (Fig. 5a). Because $t_{\text{dielectric}}$ determines the overall reflection colors, spatially selective PBVE etching by the RIE process produces a wide color range of flower patterns (Fig. 5b and Supplementary Fig. S8). The top Pd, as a trans-reflective layer, can be replaced by other perforated metal films, including Au or silver (Ag), as they maintain color changes by the water-forming reaction (Supplementary Fig. S9). However, we choose the top Pd metal for its enhanced sensitivity on H_2

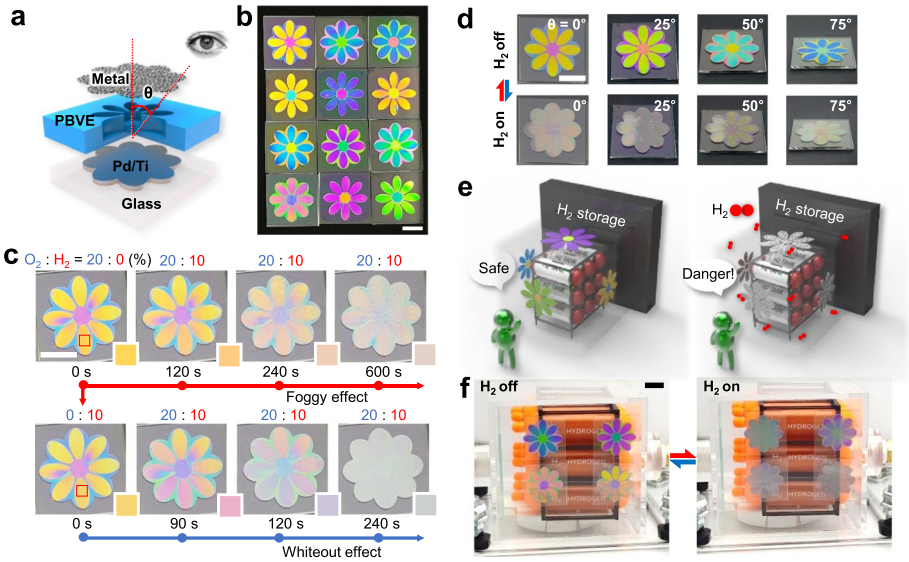

Fig. 5 Patterned FP etalon on transparent substrate for H_2 leakage warning display. **a**, **b** Schematic layer description (**a**) and photograph (**b**) of 12 fabricated f-etalon samples on glass substrate. **c** Photographs of the sample with Ag top film displaying color variation in response to different gas composition. **d** Angle-dependent color variation and foggy effect under H_2 exposure. **e**, **f** Scheme of f-etalon on glass applied for H_2 leakage warning window (**e**) and its demonstration in a miniaturized H_2 storage facility (**f**). Scale bars, 1 cm

detection below 7% H_2 (Figs. S5 and S10). For accomplishing water-forming-assisted color changes, a perforated top metal film is essential because the opening at the top metal layers allows gas to penetrate across the top metal layer. Figure 5c represents that the optical foggy effect (upper line; Fig. 5c) and whiteout effect (bottom line; Fig. 5c) were still available in the f-etalon having10-nm-thick Ag top metal, compared with the same color-changing behavior at the f-etalon with 10-nm-thick top Pd. For instance, the reference color of the f-etalon (red square of yellowish flower petals in Fig. 5c) gradually faded and then shrouded by a pale gray color at 600 s (foggy effect). Meanwhile, the yellow color of the identical zone turned white within 240 s (whiteout effect) after O_2 injection (Supplementary Video 4).

Structural color intrinsically produces angle-dependent color variation due to its increased optical path length in the resonating dielectric film. The etalon color varied with increasing viewing angle (from 0° to 75°), resembling the effect of thickening the optical cavity. Because the diffuse reflection by water bubbles is angle-independent, the foggy effect can occur at any viewing angle (Fig. 5d), making the proposed etalon structure applicable to gas leakage warning smart windows. As schematically demonstrated in Fig. 5e, the f-etalons installed in a hydrogen gas storage facility can instinctively recognize the leakage of H_2 gas by dimming the original colors of the flower patterns. This scenario was demonstrated using an actual miniature model by placing four f-etalon samples inside a miniature gas tank storage room (Fig. 5f and Supplementary Video 5).

Conclusion

Water-forming reactions and O_2 species in the air have been considered as interrupting side reactions and impurities to avoid H_2 storage and sensing technologies [43]. Here, these unwanted phenomena were applied to make the molecular reaction of H_2 and O_2

visible by transducing the gas-matter reaction into light-matter interactions over the Pd catalyst. In the transducing process, the formation of an H_2O film at the PBVE/Pd interface is critical in dynamic coloration as it determines the overall $t_{dielectric}$ constant. Previous reports demonstrated simultaneous generation and subsequent nanoscale H_2O products using electro-potential devices [22. 23]. Recently, optical monitoring of such H_2O films and their 2-dimensional growth were imaged between a vitreous silicon dioxide (SiO_2) bilayer and ruthenium [44]. However, observation of the local position and growth rates of H_2O film formation is prohibited, eliminating any possible measurement for quantitative analysis of the transition metals.

Thus, the strategic passivation of deformable PBVE films over bottom Pd metals allows H_2O products to accumulate at the microscopic level via successive growth or coalescence processes. The selection of a gas-permeable polymer membrane as a dielectric film plays multifunctional roles: i) a physical layer retarding H_2O evaporation once they are generated at the PBVE/Pd interface, ii) a dielectric layer allowing transmission of the incident light, and iii) reliable detection performance even in a humid environment which is one of the chronic hurdles of electrically biased H_2 sensors [45]. Applying a perforated top metal film is essential for creating structural colors by its efficient transreflective characteristic yielding the FP resonating effect and for allowing gas penetration through the nano-apertures of the metal film. There was no color change under H_2/O_2 exposure when the top Pd was nanohole-less, which confirms that the perforated metal film is key for dynamic coloration, as it allows gas reactants and products to cross the metal film (Supplementary Fig. S3 and S9).

Leveraging the underlying principle of the FP resonator, the in situ tracking of different types of H_2O products was optically realized via gas stimulus-induced dynamic optical coloration. Based on the color variation as a function of dielectric changes, we experimentally observed exotic optical phenomena: the water bubble-assisted 'optical foggy effect' and the water film-assisted 'optical whiteout effect'. Quantitative analysis of H_2O production/desorption has been achieved only by mass spectrometry [46]. But no further information has been provided, such as tracking chemical reaction pathways. Our dynamic optical coloration technology provides information on how H_2 and O_2 react at the PBVE/Pd interface and allows the tracking of gas-matter physical/chemical interaction behaviors using simple spectroscopy and naked-eye monitoring methods.

Hydrogenation has been investigated using diverse materials to realize repeatable and reliable coloration devices. Mg or Y, as representative hydrogen absorbents, showed phase transformation from the metallic phase to dielectric MgH_2 or YH_X, as it promotes dynamic plasmonic coloration with remarkable variations in reflectance spectra [37, 47]. However, these coloration techniques are highly dependent on material properties and have insuperable disadvantages such as low switching speed, inferior color tunability, and low color efficiency. Although the induced phase change of the gas-sensitive Mg-assisted FP etalon is the most sophisticated and advanced dynamic coloration technology to date, it still suffers from material stability and safety issues when exposed to moisture (humid environment) which is crucial for industrial applications. Additionally, it ignites and emits combustible gases (such as magnesium nitride) or flashes with intense ultraviolet rays, which can be fatal to humans. Moreover, Mg can ignite when in contact with silica, complicating Mg use as a color display that uses SiO_2 substrates.

Thus, Y can be used as an alternative gas absorbent at room temperature. However, Mg and Y require the additional deposition of Pd or platinum catalyst layers to complement their deficient hydrogen adsorption/dissociation properties. Frank et al. also reported restricted cycling numbers (< 20 times) of metal hydride-based dynamic color tunings [41]. Unlike any other dynamic color tuning strategy using metal hydride-based reports, our FP etalon shows superior stability ($\geq$ 28 times, as shown in Fig. 3i) of the device structures. The advanced repetition without active metal damage is because the color change did not originate from the direct reaction of the Pd/PdH_X transition but the water-forming reaction at the PBVE/Pd interfaces. Furthermore, Pd nanoparticles have been combined with Au nanoparticles to apply their plasmonic effect in hydrogen sensing. Differ from them, the larger resonance shifts up to 300 nm enable us to realize an eye-readable colorimetric sensor that operates even in the real-world environments where O_2 is present, as compared to higher-sensitive hydrogen sensors that work under restricted measurement conditions [48, 49].

Overall, employing the colorimetric display for monitoring different chemical reactions at catalytic interfaces creates numerous opportunities to clarify the underlying physics, chemistry, and applied surface chemistry assisted by optoelectronic nanostructures. For example, the advanced photonic measurement for the 'membrane permeability test' of polymers of interest. Without state-of-the-art imaging instruments, we can simply monitor the pathway solely on color variation. Smart windows for air quality monitoring or gas leaking warning displays can be other applicable areas as they meet industrial needs owing to their scalable and simple fabrication process with diverse solid supports and various metal selections.

Methods

Fabrication of FP etalon substrates

On a Si wafer, a 10 nm Ti adhesion layer and 10 nm Pd layer were subsequently deposited using a thermal evaporator (MHS-1800, Muhan; 10^{-7} Torr; 3.0 Å/s). A PBVE polymer mixture was prepared by diluting 9.0 wt.% PBVE polymer (Chromis Technologies, USA) in a fluoro-solvent (FC-43, Chromis Technologies, USA) to obtain 6.0 wt.%, and then spin-coated on the Pd surface at 900 rpm for 30 s. To eliminate air bubbles inside the mixture, it was placed at room temperature for 1 h and baked on a hotplate at 50 °C, 80 °C, and 180 °C for 1 h each in order, resulting in a 590 nm thick PBVE layer. The polymer layer was delicately etched using RIE (RIE 80 plus, Oxford Instrument) to modify the thicknesses of the different colors. Spatially selective etching process was achieved using an information-perforated shadow mask at an etching rate of $\approx$ 3.5 $nm{\cdot}s^{-1}$ (5×10^{-2} Torr pressure, RF power of 3 W, and O_2 gas flow rate of 10 sccm). Before top Pd deposition, the high surface energy of the PBVE film was relieved by annealing at 180 °C for 30 min. Subsequently, 15 nm of the top Pd layer was thermally deposited on the PBVE film.

FLIC pattern analysis and thickness simulation

To uniformly cover the PBVE with a thin calcein layer, O_2 plasma surface treatment (CUTE, Femto Science, Korea) was applied to enhance the surface energy. Then, 6.4×10^{-4} M of calcein (TCI) dissolved in dimethyl sulfoxide (Sigma-Aldrich) was then

spin-coated on the PBVE surface at 4500 rpm for 60 s, followed by N_2 blow drying. While a gas mixture of 10% of H_2 and 20% of O_2 in N_2 carrier gas was supplied to the gas chamber, the fringe patterns on the sample surface were monitored with a microscope using FITC filters. Fluorescence intensity profiles were measured to examine the water bubble height. Further details on the bubble height simulation are provided in Supplementary Note 3.

Gas control and optical analysis

To control the H_2 concentration, a mass flow controller (MFC) was used for each gas. To realize the atmospheric conditions, a 1:4 ratio of O_2 and N_2 was maintained for the carrier gas. The experimental setup is shown in Supplementary Fig. S8. The outlet of the chamber was connected to a hydrogen concentration analyzer (EN-600, Shanghai ENCEL Instrument Co., Ltd.) to monitor the real-time H_2 concentration inside the chamber. The reflectance spectrum was measured using ultraviolet–visible spectroscopy (USB4000-UV–VIS, Ocean Optics) with normal incident white light (DH-MINI, Ocean Optics) and a reflection probe (R400-7-SR, Ocean Optics).

Abbreviations

DFT	Density functional theory
FP	Fabry-Perot
PBVE	Perfluoro-(butenyl vinyl ether)
PMMA	Polymethyl methacrylate
FLIC	Fluorescence interference contrast microscopy
FL	Fluorescence
FITC	Fluorescein isothiocyanate
MDM	Metal-dielectric-metal
RI	Refractive index
SEM	Scanning electron microscopy
RIE	Reactive ion etching
MFC	Mass flow controller

Supplementary Information

The online version contains supplementary material available at https://doi.org/10.1186/s43074-023-00097-1.

Additional file 1: Supplementary Note 1. DFT calculations. **Supplementary Note 2.** Polymer dielectric control experiments. **Figure S1.** Effect of gas permeability of the polymer dielectric on water-forming reaction and following spectral response. **Supplementary Note 3.** FLIC simulation and fitting. **Figure S2.** Expected interference patterns and FL intensity depending on the water bubble height. **Supplementary Note 4.** Optical simulation. **Figure S3.** Filling fraction and color coverage depending on top Pd thickness. **Supplementary Note 5.** FP etalon fabrication process and color map. **Figure S4.** Fabrication process and structural color generations. **Figure S5.** Measured optical response of a Pd-PBVE-Pd etalon varying H_2 concentration. **Figure S6.** Mechanical durability of PBVE film during repeated water-forming reactions. **Supplementary Note 6**. Spectral simulation for water film increment. **Figure S7.** Spectral behavior depending on $t_{dielectric}$. **Figure S8.** Dielectric thickness information of f-etalons. **Figure S9.** The f-etalons prepared with different top metals with various filling fraction. **Figure S10.** Measured optical response of a Au-PBVE-Pd etalon varying H_2 concentrations. **Figure S11.** Experimental set-up.

Additional file 2: Supplementary Video 1. Water-bubble formation.

Additional file 3: Supplementary Video 2. H_2 gas response of Pd etalon.

Additional file 4: Supplementary Video 3. O_2 gas response of PdH etalon (Under 10% H_2).

Additional file 5: Supplementary Video 4. Flower-MDM etalon on glass (Ag top metal).

Additional file 6: Supplementary Video 5. H_2 gas leakage warning window demonstration.

Acknowledgements

We acknowledge support from Prof. Sin-Doo Lee (Department of Electrical and Computer Engineering, Seoul National University) for his scientific counsel and advice that improves the depth of our work.

Authors' contributions
J.L. conceived the study, fabricated the devices, and analyzed the data. E.-S.Y. designed and conducted optical simulation. T.K. and I.S.K. assisted with device fabrication and optical measurement. S.C. assisted with the gas exposure experiment. S.J.K. and W.B.L. conduced DFT simulation. Y.P. and Y.-S.R. wrote the manuscript and supervised work. All authors contributed to the scientific discussion and manuscript revisions.

Funding
This work was supported by a National Research Foundation of Korea (NRF) grant funded by the Korean government (MSIT) (No. 2021R1A2C2009236 and No. 2020M3H5A108110413). Y.-S.R. acknowledges support from a grant of the Information and Communications Promotion Fund (ICT promotion fund) through the National IT Industry Promotion Agency (NIPA), and Korea University Grant (K2311801). Y.P acknowledges support from KIST Institutional grants (No. 2E32451 and 2V09640).

Availability of data and materials
The datasets used and/or analyzed during the current study are available from the corresponding authors on reasonable request.

Declarations

Competing interests
The authors declare that they have no competing interests.

Received: 5 December 2022 Revised: 2 May 2023 Accepted: 30 May 2023
Published online: 26 June 2023

References

1. Tang L, Li J. Plasmon-based colorimetric nanosensors for ultrasensitive molecular diagnostics. ACS Sens. 2017;2(7):857–75. https://doi.org/10.1021/acssensors.7b00282.
2. Ajay Piriya VS, Joseph P, Kiruba Daniel SCG, Lakshmanan S, Kinoshita T, Muthusamy S. Colorimetric sensors for rapid detection of various analytes. Mater Sci Eng C. 2017;78:1231–45. https://doi.org/10.1016/j.msec.2017.05.018.
3. Aldewachi H, Chalati T, Woodroofe M, Bricklebank N, Sharrack B, Gardiner P. Gold nanoparticle-based colorimetric biosensors. Nanoscale. 2018;10(1):18–33. https://doi.org/10.1039/C7NR06367A.
4. Liu B, Zhuang J, Wei G. Recent advances in the design of colorimetric sensors for environmental monitoring. Environ Sci Nano. 2020;7(8):2195–213. https://doi.org/10.1039/D0EN00449A.
5. Nguyen QH, Kim MI. Using nanomaterials in colorimetric toxin detection. Biochip J. 2021;15(2):123–34. https://doi.org/10.1007/s13206-021-00013-4.
6. Shu FZ, Yu FF, Peng RW, Zhu YY, Xiong B, Fan RH, et al. Dynamic plasmonic color generation based on phase transition of vanadium dioxide. Adv Opt Mater. 2018;6(7):1700939. https://doi.org/10.1002/adom.201700939.
7. Fudouzi H, Sawada T. Photonic rubber sheets with tunable color by elastic deformation. Langmuir. 2006;22(3):1365–8. https://doi.org/10.1021/la0521037.
8. Jung C, Kim S-J, Jang J, Ko JH, Kim D, Ko B, et al. Disordered-nanoparticle-based etalon for ultrafast humidity-responsive colorimetric sensors and anti-counterfeiting displays. Sci Adv. 2022;8(10):598. https://doi.org/10.1126/sciadv.abm8598.
9. de la Rica R, Stevens MM. Plasmonic ELISA for the ultrasensitive detection of disease biomarkers with the naked eye. Nat Nanotechnol. 2012;7(12):821–4. https://doi.org/10.1038/nnano.2012.186.
10. Duan X, Liu N. Scanning plasmonic color display. ACS Nano. 2018;12(8):8817–23. https://doi.org/10.1021/acsnano.8b05467.
11. Andringa AM, Meijboom JR, Smits EC, Mathijssen SG, Blom PW, de Leeuw DM. Gate-bias controlled charge trapping as a mechanism for NO_2 detection with field-effect transistors. Adv Funct Mater. 2011;21:100–7.
12. Georg A, Georg A, Graf W, Wittwer V. Switchable windows with tungsten oxide. Vacuum. 2008;82(7):730–5. https://doi.org/10.1016/j.vacuum.2007.10.020.
13. Huiberts J, Griessen R, Rector J, Wijngaarden R, Dekker J, de Groot D, et al. Yttrium and lanthanum hydride films with switchable optical properties. Nature. 1996;380(6571):231–4. https://doi.org/10.1038/380231a0.
14. Palm KJ, Murray JB, Narayan TC, Munday JN. Dynamic optical properties of metal hydrides. ACS Photonics. 2018;5(11):4677–86. https://doi.org/10.1021/acsphotonics.8b01243.
15. Nørskov JK, Abild-Pedersen F, Studt F, Bligaard T. Density functional theory in surface chemistry and catalysis. Proc Natl Acad Sci. 2011;108(3):937–43. https://doi.org/10.1073/pnas.1006652108.
16. Rotermund H, Ertl G, Sesselmann W. Scanning photoemission microscopy of surfaces. Surf Sci. 1989;217(3):L383–90. https://doi.org/10.1016/0039-6028(89)90428-7.
17. Telieps W, Bauer E. An analytical reflection and emission UHV surface electron microscope. Ultramicroscopy. 1985;17(1):57–65. https://doi.org/10.1016/0304-3991(85)90177-9.
18. Dicke J, Rotermund H, Lauterbach J. Ellipsomicroscopy for surface imaging: contrast mechanism, enhancement, and application to CO oxidation on Pt (110). J Opt Soc Am A. 2000;17(1):135–41. https://doi.org/10.1364/JOSAA.17.000135.
19. Dicke J, Erichsen P, Wolff J, Rotermund H. Reflection anisotropy microscopy: improved set-up and applications to CO oxidation on platinum. Surf Sci. 2000;462(1–3):90–102. https://doi.org/10.1016/S0039-6028(00)00571-9.
20. Yuan W, Zhu B, Li X, Hansen TW, Ou Y, Fang K, et al. Visualizing H_2O molecules reacting at TiO_2 active sites with transmission electron microscopy. Science. 2020;367(6476):428–30. https://doi.org/10.1126/science.aay2474.

21. Dannetun HM, Söderberg D, Lundström I, Petersson L. The H_2–O_2 reaction on palladium studied over a large pressure range: Independence of the microscopic sticking coefficients on surface condition. Surf Sci. 1985;152:559–68. https://doi.org/10.1016/0039-6028(85)90188-8.
22. Petersson L, Dannetun HM, Lundström I. The water-forming reaction on palladium. Surf Sci. 1985;161(1):77–100. https://doi.org/10.1016/0039-6028(85)90729-0.
23. Petersson L, Dannetun HM, Lundström I. Water production on palladium in hydrogen-oxygen atmospheres. Surf Sci. 1985;163(1):273–84. https://doi.org/10.1016/0039-6028(85)90864-7.
24. Roques J, Lacaze-Dufaure C, Mijoule C. Dissociative adsorption of hydrogen and oxygen on palladium clusters: a comparison with the (111) infinite surface. J Chem Theory Comput. 2007;3(3):878–84. https://doi.org/10.1021/ct600370g.
25. El-Okazy MA, Liu L, Junk CP, Kathmann E, White W, Kentish SE. Gas separation performance of copolymers of perfluoro (butenyl vinyl ether) and perfluoro (2, 2-dimethyl-1, 3-dioxole). J Membr Sci. 2021;634:119401. https://doi.org/10.1016/j.memsci.2021.119401.
26. Kim KR, Noh J, Lee JM, Kim YJ, Lee W. Suppression of phase transitions in Pd thin films by insertion of a Ti buffer layer. J Mater Sci. 2011;46(6):1597–601. https://doi.org/10.1007/s10853-010-4970-x.
27. Nyberg C, Tengstål C. Adsorption and reaction of water, oxygen, and hydrogen on Pd (100): identification of adsorbed hydroxyl and implications for the catalytic H_2–O_2 reaction. J Chem Phys. 1984;80(7):3463–8. https://doi.org/10.1063/1.447102.
28. Ryu Y, Yoo D, Wittenberg NJ, Jordan LR, Lee S-D, Parikh AN, et al. Lipid membrane deformation accompanied by disk-to-ring shape transition of cholesterol-rich domains. J Am Chem Soc. 2015;137(27):8692–5. https://doi.org/10.1021/jacs.5b04559.
29. Vaughan JM. The Fabry-Perot interferometer: history, theory, practice and applications. Oxford: Routledge; 2017.
30. Yu E, Lee SH, Bae YG, Choi J, Lee D, Kim C, et al. Highly sensitive color tunablility by scalable nanomorphology of a dielectric layer in liquid-permeable metal-insulator-metal structure. ACS Appl Mater Interfaces. 2018;10(44):38581–7. https://doi.org/10.1021/acsami.8b12553.
31. Jeong H, Lee J, Yu E, Kim T, Kim IS, Lee S, et al. Physicochemical modulation of nanometer-thick etalon films for liquid-sensitive color display with full-color spectrum generation. ACS Appl Nano Mater. 2020;4(1):389–95. https://doi.org/10.1021/acsanm.0c02746.
32. Kim T, Yu E, Bae Y, Lee J, Kim IS, Chung S, et al. Asymmetric optical camouflage: tuneable reflective colour accompanied by the optical Janus effect. Light Sci Appl. 2020;9(1):1–10. https://doi.org/10.1038/s41377-020-00413-5.
33. Yu E, Chae K, Kim T, Lee J, Seo J, Kim IS, et al. Development of a photonic switch via electro-capillarity-induced water penetration across a 10-nm gap. Small. 2022;18:2107060. https://doi.org/10.1002/smll.202107060.
34. Seal K, Genov D, Sarychev A, Noh H, Shalaev VM, Ying Z, et al. Coexistence of localized and delocalized surface plasmon modes in percolation metal films. Phy Rev Lett. 2006;97(20):206103. https://doi.org/10.1103/PhysRevLett.97.206103.
35. Maaroof A, Sutherland D. Optimum plasmon hybridization at percolation threshold of silver films near metallic surfaces. J Phys D Appl Phys. 2010;43(40):405301. https://doi.org/10.1088/0022-3727/43/40/405301.
36. Sharma G, Bala R. Digital color imaging handbook. Boca Raton: CRC Press; 2017.
37. Ngene P, Radeva T, Slaman M, Westerwaal RJ, Schreuders H, Dam B. Seeing hydrogen in colors: low-cost and highly sensitive eye readable hydrogen detectors. Adv Funct Mater. 2014;24(16):2374–82. https://doi.org/10.1002/adfm.201303065.
38. Johnson NJJ, Lam B, MacLeod BP, Sherbo RS, Moreno-Gonzalez M, Fork DK, et al. Facets and vertices regulate hydrogen uptake and release in palladium nanocrystals. Nat Mater. 2019;18(5):454–8. https://doi.org/10.1038/s41563-019-0308-5.
39. Namba K, Ogura S, Ohno S, Di W, Kato K, Wilde M, et al. Acceleration of hydrogen absorption by palladium through surface alloying with gold. Proc Natl Acad Sci. 2018;115(31):7896–900. https://doi.org/10.1073/pnas.1800412115.
40. Langmuir I. The constitution and fundamental properties of solids and liquids. II Liquids J Am Chem Soc. 1917;39(9):1848–906. https://doi.org/10.1021/ja02254a006.
41. Neubrech F, Duan X, Liu N. Dynamic plasmonic color generation enabled by functional materials. Sci Adv. 2020;6(36):eabc2709. https://doi.org/10.1126/sciadv.abc2709.
42. Baldi A, Narayan TC, Koh AL, Dionne JA. In situ detection of hydrogen-induced phase transitions in individual palladium nanocrystals. Nat Mater. 2014;13(12):1143–8. https://doi.org/10.1038/nmat4086.
43. Zhang T, Ling C, Xue Q, Wu T. The effect of oxygen molecule on the hydrogen storage process of Li-doped graphene. Chem Phys Lett. 2014;599:100–3. https://doi.org/10.1016/j.cplett.2014.03.035.
44. Prieto MJ, Klemm HW, Xiong F, Gottlob DM, Menzel D, Schmidt T, et al. Water formation under silica thin films: real-time observation of a chemical reaction in a physically confined space. Angew Chem Int Ed. 2018;57(28):8749–53. https://doi.org/10.1002/anie.201802000.
45. Hashtroudi H, Kumar R, Savu R, Moshkalev S, Kawamura G, Matsuda A, et al. Hydrogen gas sensing properties of microwave-assisted 2D Hybrid Pd/rGO: Effect of temperature, humidity and UV illumination. Int J Hydrog Energy. 2021;46(10):7653–65. https://doi.org/10.1016/j.ijhydene.2020.11.268.
46. Petersson L, Dannetun HM, Lundström I. Hydrogen detection during catalytic surface reactions: evidence for activated lateral hydrogen mobility in the water-forming reaction on Pd. Phys Rev Lett. 1984;52(20):1806–9. https://doi.org/10.1103/PhysRevLett.52.1806.
47. Duan X, Kamin S, Liu N. Dynamic plasmonic colour display. Nat Commun. 2017;8(1):1–9. https://doi.org/10.1038/ncomms14606.
48. Syrenova S, Wadell C, Langhammer C. Shrinking-hole colloidal lithography: self-aligned nanofabrication of complex plamonic nanoantennas. Nano Lett. 2014;14(5):2655–63. https://doi.org/10.1021/nl500514y.
49. Yang A, Huntington MD, Cardinal MF, Masango SS, Van Duyne RP, Odom TW. Hetero-oligomer nanoaparticle arrays for plasmon-enhanced hydrogen sensing. ACS Nano. 2014;8(8):7639–47. https://doi.org/10.1021/nn502502r.

Publisher's Note